

Buckling analysis of stiffened plate structures by an improved meshfree flat shell formulation

S. Sadamoto^a, S. Tanaka^a, K. Taniguchi^a, M. Ozdemir^{b,c},
T.Q. Bui^d, C. Murakami^e, D. Yanagihara^f

^a*Graduate School of Engineering, Hiroshima University, Japan,
e-mail: shota.sadamoto@gmail.com, satoyuki@hiroshima-u.ac.jp,
m166479@hiroshima-u.ac.jp*

^b*Faculty of Naval Architecture and Ocean Engineering,
Istanbul Technical University, Turkey, e-mail: mozdemir@itu.edu.tr*

^c*Faculty of Marine Science, Ordu University, Turkey*

^d*Department of Civil and Environmental Engineering,
Tokyo Institute of Technology, Japan, e-mail: tinh.buiquoc@gmail.com*

^e*National Maritime Research Institute, Japan, e-mail: c_murak@nmri.go.jp*

^f*Graduate School of Science and Engineering, Ehime University,
Japan, e-mail: dais@ehime-u.ac.jp*

Abstract

An efficient Galerkin meshfree flat shell formulation is presented for the analysis of buckling behaviors of stiffened plate structures. Both plate bending and membrane deformations are approximated by the reproducing kernel particle method (RKPM). The governing equation is transformed into a weak form, and it is discretized by the scattered nodes. The stiffness matrix is numerically integrated with the nodal integration technique, *i.e.*, the stabilized conforming nodal integration (SCNI). The RKPM and SCNI based flat shell modeling approach can address the shear locking problem. Additionally, the present discretization is further improved by involving a drilling rotation component, which is to effectively model the stiffeners. There are six degrees of freedom per node. A singular kernel is also introduced into a set of the interpolants to model the web/flange connection, as well as the imposition of the essential boundary conditions. A generalized eigenvalue problem is analyzed for evaluating buckling loads/modes of the stiffened plate structures. The accuracy of the numerical results and the effectiveness of the proposed method are examined through several numerical examples.

Keywords: Meshfree, Reproducing Kernel, Stiffened Plate, Buckling

1. Introduction

A ship's hull structure is subjected to longitudinal bending induced by external loads, *e.g.*, self-weight, cargo weights and wave forces. The hull structure is generally composed of plates, stiffeners and stiffened plate structures [1-4]. It is important to design the structural members optimally, by choosing the thickness and aspect ratio of the plating as well as size of the web/flange and the number of stiffeners to prevent the occurrence of the structural failures within a limited construction expense. Many researches have been performed on the evaluation of buckling loads/modes and found the ultimate strength for the stiffened plate and hull structures, *e.g.*, see Refs. [5-10]. The present study focuses on buckling analysis of the plate and stiffened plate structures, by employing a novel numerical simulation method.

In recent years, meshfree and other related methodologies, *e.g.*, the element free Galerkin method (EFGM) [11], the reproducing kernel particle method (RKPM) [12], the extended finite element method [13,14], the isogeometric analysis [15-18], and the wavelet Galerkin method [19-23], have been widely adopted to analyze scientific and engineering problems. Meshfree method is particularly attractive for the analysis of plate and shell structures. Continuous functions can be used to approximate the deflection and rotational components, smooth stress/strain distributions are obtained throughout the entire analysis domain, and the shear locking problem can also be avoided. Krysl and Belytschko [24, 25] analyzed plate and shell problems by employing the EFGM. Noguchi *et al.* [26] solved shell and spatial structures by EFGM employing a convected coordinate system. Kanok-Nukulchai *et al.* [27] examined the shear locking property of meshfree plate bending problems. Generally, plate and shell problems with flat or smoothly curved surfaces were modeled by the meshfree method because a special treatment is required to address the displacement discontinuity or its derivative. Zhang *et al.* [28] analyzed shell structures with discontinuities employing a moving least-square approximation with a discontinuous derivative function. Tanaka *et al.* [29-31] treated the displacement discontinuity of a cracked shear deformable plate by modifying the reproducing kernel (RK) interpolation functions along the crack segment with a diffraction method and a visibility criterion [32,33].

An efficient Galerkin meshfree method is presented here to analyze buck-

ling behaviors of assembled plate structures such as a stiffened plate structure. A flat shell formulation is employed based on the RK approximation [12,34-37]. Mindlin-Reissner plate formulation is adopted to represent the plate bending deformation, and plane stress condition is assumed for the membrane deformation. The in-plane and out-of-plane deformations are coupled and approximated by the RKs. The flat shell is modeled by the scattered nodes, and the stabilized conforming nodal integration (SCNI) [38,39] is employed to accurately integrate the stiffness matrices with the Voronoi cell diagram [40]. The flat shell modeling on the basis of the RKPM and SCNI can overcome the shear locking problem by imposing a so-called Kirchhoff mode reproducing condition (KMRC) [41,42]. Wang and Sun [43] and Sadamoto *et al.* [44] analyzed geometrically nonlinear problems for the flat shells. Yoshida *et al.* [45] succeeded in producing a linear buckling analysis of a flat shell model including curved stiffeners. The flat shell modeling involves five degrees of freedom (5DOFs) per node, and the stiffeners were modeled by suppressing the deflection components of the flat shell model. Curved shell problems were also analyzed in [46].

In the present research, a drilling rotation component is included to model stiffeners efficiently. Therefore, the meshfree discretization possesses six degrees of freedom (6DOFs) per node. Because the drilling component does not have any resisting force or stiffness, a penalty energy function proposed by Kanok-Nukulchai [47] is introduced. In the author's previous study, a multiple point constraint (MPC) technique was adopted for the meshfree web/flange modeling and imposition of the essential boundary conditions in [48]. However, stress oscillation was found along the boundary conditions in the MPC enforcements [44]. A singular kernel (SK) [49] is then applied to impose the so-called Kronecker delta function property in the set of the meshfree interpolants. Additionally, sub-domain stabilized conforming integration (SSCI) [50-55] is employed for evaluating the stiffness matrices around the web/flange connections. So far, research has been conducted to analyze the buckling behaviors of the plates and assembled plate structures using meshfree and related methods in [56-66]. The modeling of stiffened plate structures based on RKPM and SCNI, and high accuracy buckling loads/modes evaluations have not been reported yet. The mathematical formulation and discretization of the proposed method are presented for analyzing the stiffened plate structures. The calculated results are critically examined through the numerical examples.

The contents of this paper is as follows. The meshfree flat shell formu-

lation including the drilling rotation component and the nodal integration techniques are presented in Chapter 2. Modeling of the stiffened plate structures is discussed in Chapter 3. Numerical examples for several buckling problems for plate and stiffened plate structures are presented in Chapter 4. Conclusions are given in Chapter 5.

2. Meshfree modeling for a flat shell

2.1. Governing equations for linear buckling analysis

When simulating buckling behaviors of plate structures, the plate bending deformation, in contrast to the membrane deformation, cannot be neglected. A flat shell formulation is developed by combining the in-plane and out-of-plane deformations. A schematic flat shell model is represented in Fig.1. S is the area of plate and t_h is the plate thickness. A plane stress condition and Mindlin-Reissner plate theory are adopted to allow shear deformation of the plate. The membrane deformations in the x_1 - and x_2 -directions at the mid-thickness plane are represented by u_{1mid} and u_{2mid} , respectively, the deflection component of the plate is represented by u_3 , and the rotational angles for the x_1 - and x_2 -axes are represented by θ_1 and θ_2 , respectively. θ_3 is the drilling rotation component.

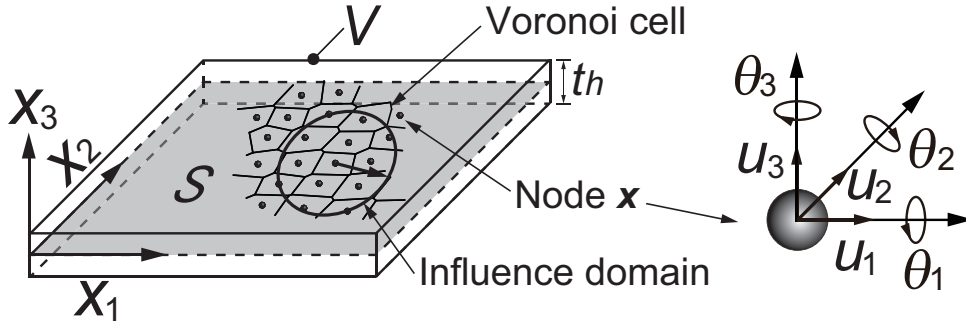


Figure 1: A schematic illustration of a flat shell and its meshfree discretization.

The plate deformation $\mathbf{u}(\mathbf{x})$ can be expressed as:

$$\mathbf{u}(\mathbf{x}) = \begin{Bmatrix} u_1(\mathbf{x}) \\ u_2(\mathbf{x}) \\ u_3(\mathbf{x}) \end{Bmatrix} = \begin{Bmatrix} u_{1mid}(\mathbf{x}) + z\theta_2(\mathbf{x}) \\ u_{2mid}(\mathbf{x}) - z\theta_1(\mathbf{x}) \\ u_3(\mathbf{x}) \end{Bmatrix}, \quad (1)$$

where $u_k(\mathbf{x})$ ($k=1, 2, 3$) are components of the displacement toward the x_k -axes. z ($|z| \leq t_h/2$) represents the distance from the mid-thickness plane of the plate.

When considering an elastic stability problem of a shear deformable plate, the following weak form can be obtained:

$$\int_V \boldsymbol{\sigma} : \delta \boldsymbol{\varepsilon}_L dV + \lambda \int_V \boldsymbol{\sigma}'_0 : \delta \boldsymbol{\varepsilon}_{NL} dV = 0, \quad (2)$$

where $\boldsymbol{\varepsilon}_L$ and $\boldsymbol{\varepsilon}_{NL}$ are the linear and nonlinear strain tensors. δ represents variational operator. V is the volume of the plate. The linear strain components ε_{Lij} ($=\boldsymbol{\varepsilon}_L$) can be described as:

$$\begin{pmatrix} \varepsilon_{L11} \\ \varepsilon_{L22} \\ 2\varepsilon_{L12} \\ 2\varepsilon_{L31} \\ 2\varepsilon_{L23} \end{pmatrix} = \begin{pmatrix} \frac{\partial u_{1mid}}{\partial x_1} + z \frac{\partial \theta_2}{\partial x_1} \\ \frac{\partial u_{2mid}}{\partial x_2} - z \frac{\partial \theta_1}{\partial x_2} \\ \frac{\partial u_{1mid}}{\partial x_2} + \frac{\partial u_{2mid}}{\partial x_1} + z \left(\frac{\partial \theta_2}{\partial x_2} - \frac{\partial \theta_1}{\partial x_1} \right) \\ \frac{\partial u_3}{\partial x_1} + \theta_2 \\ \frac{\partial u_3}{\partial x_2} - \theta_1 \end{pmatrix}. \quad (3)$$

The nonlinear strain tensor $\boldsymbol{\varepsilon}_{NL}$ is defined as:

$$\varepsilon_{NLij} = \frac{1}{2} \left(\frac{\partial u_k}{\partial x_i} \frac{\partial u_k}{\partial x_j} \right). \quad (4)$$

Additionally, $\boldsymbol{\sigma} = \{\sigma_{11} \ \sigma_{22} \ \sigma_{12} \ \sigma_{31} \ \sigma_{23}\}^T$ is the Cauchy stress tensor. The stress-strain relationship can be written as $\mathbf{D}\boldsymbol{\varepsilon}_L$, and the elastic coefficient matrix \mathbf{D} for the shear deformable plate is written as:

$$\mathbf{D} = \frac{E}{1-\nu^2} \begin{bmatrix} 1 & \nu & 0 & 0 & 0 \\ \nu & 1 & 0 & 0 & 0 \\ 0 & 0 & \frac{1-\nu}{2} & 0 & 0 \\ 0 & 0 & 0 & \kappa \frac{1-\nu}{2} & 0 \\ 0 & 0 & 0 & 0 & \kappa \frac{1-\nu}{2} \end{bmatrix}, \quad (5)$$

where κ is the shear correction factor, and $\kappa = \pi^2/12$ is adopted. E is the Young's modulus and ν is the Poisson's ratio. $\boldsymbol{\sigma}'_0$ is a pre-buckling stress tensor which is represented as:

$$\boldsymbol{\sigma}'_0 = \begin{bmatrix} \sigma'_{011} \mathbf{I} & \sigma'_{012} \mathbf{I} & \sigma'_{013} \mathbf{I} \\ \sigma'_{021} \mathbf{I} & \sigma'_{022} \mathbf{I} & \sigma'_{023} \mathbf{I} \\ \sigma'_{031} \mathbf{I} & \sigma'_{032} \mathbf{I} & \mathbf{0} \end{bmatrix}, \quad (6)$$

where \mathbf{I} is a 3×3 unit tensor. σ'_{033} is set as zero based on the plane stress assumption.

2.2. A RKPM meshfree approximation of a flat shell

In the meshfree discretization, nodes are distributed on the mid-thickness plane of the plate as shown in Fig.1. The physical quantities are approximated by a linear combination of the RK functions. Each node has 6DOFs, *i.e.*, three in-plane deformation components ($u_{1mid}, u_{2mid}, \theta_3$) and three out-of-plane deformation components (u_3, θ_1, θ_2), respectively. The 6DOFs are denoted as: $\{u_{1mid} \ u_{2mid} \ u_3 \ \theta_1 \ \theta_2 \ \theta_3\}^T = \{u_1 \ u_2 \ u_3 \ u_4 \ u_5 \ u_6\}^T$. The vector components $u_i^h(\mathbf{x})$ ($i=1, \dots, 6$) ($=\mathbf{u}^h(\mathbf{x})$) are represented by RK $\psi_I(\mathbf{x})$ ($I=1, \dots, NP$) as:

$$u_i^h(\mathbf{x}) = \sum_{I=1}^{NP} \psi_I(\mathbf{x}) u_{iI}, \quad (i = 1, \dots, 6), \quad (7)$$

where u_{iI} represents the coefficient vector for each component and NP is total number of nodes to be used for the approximation. The RK function $\psi_I(\mathbf{x})$ is constructed from the original kernel function $\phi_I(\mathbf{x})$ to impose the so-called reproducing condition (RC). It is represented by a basis vector $\mathbf{h}(\mathbf{x})$ and its coefficient vector $\mathbf{b}(\mathbf{x})$ as:

$$\psi(\mathbf{x}) = \mathbf{h}^T(\mathbf{x}_I - \mathbf{x}) \mathbf{b}(\mathbf{x}) \phi_I(\mathbf{x}_I - \mathbf{x}). \quad (8)$$

Wang *et al.* [41] analyzed KMRC which is a necessary condition to address the shear locking problem in the meshfree approximation. A complete quadratic basis $\mathbf{h}(\mathbf{x}) = \{1 \ x_1 \ x_2 \ x_1^2 \ x_1 x_2 \ x_2^2\}$ is chosen as the basis vector for imposing KMRC. $\mathbf{b}(\mathbf{x})$ is a coefficient vector that satisfies the RC [12,41]. A cubic spline kernel function is used as the original kernel function $\phi_I(\mathbf{x}_I - \mathbf{x})$ as:

$$\phi_I(\mathbf{x}_I - \mathbf{x}, h) = \frac{10}{7\pi h^2} \begin{cases} 1 - \frac{3}{2}s^2 + \frac{3}{4}s^3 & (0 \leq s \leq 1) \\ \frac{1}{4}(2-s)^3 & (1 \leq s \leq 2) \\ 0 & (2 \leq s) \end{cases}, \quad (9)$$

where s ($=|\mathbf{x}_I - \mathbf{x}|/h$) is a normalized distance from the center of the kernel, and h is a parameter that determines the function support.

The original RKs do not possess the so-called Kronecker delta property, *i.e.*, $u_i^h(\mathbf{x}) \neq u_{iI}$ in Eq.(7). A SK [49] is introduced. The original RKs are modified to impose the Kronecker delta property. The approximated displacements associated with the SKs are represented as:

$$u_i^h(\mathbf{x}) = \sum_{I=1, I \neq J}^{NP} \psi_I(\mathbf{x}) u_{iI} + \tilde{\psi}_J(\mathbf{x}) u_{iJ}, \quad (i = 1, \dots, 6), \quad (10)$$

where $\tilde{\psi}_J(\mathbf{x})$ is a SK. An example of a one-dimensional (1D) arrangement for original RKs and SKs is shown in Fig.2. A highly accurate imposition of the essential boundary conditions, as well as modeling of plate-stiffener connections can be achieved by introducing the SKs.

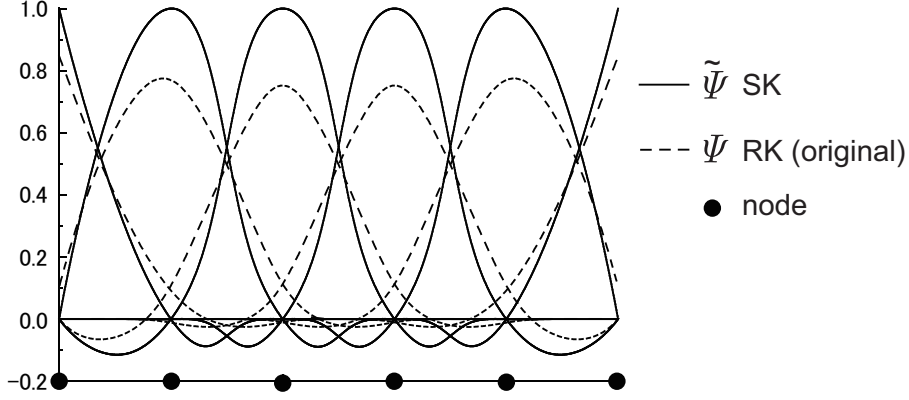


Figure 2: Shape functions comparison of 1D arrangements of the original RKs and SKs.

2.2.1. Nodal integration techniques

The SCNI and SSCI are introduced as effective numerical integration techniques to accurately evaluate the stiffness matrices in buckling analysis problems. In the meshfree discretization, nodes are distributed on the mid-thickness plane of the flat shell, and a Voronoi cell diagram is automatically generated based on the distributed nodes as shown in Fig.3(a). \mathbf{x}_K is a position vector of the K -th node, and Ω_K is a domain of the Voronoi cell. Γ_K is the boundary. The nodal integration techniques can be explained as follows. The derivatives of the components for $\tilde{u}_j^h(\mathbf{x}_K)$ ($j=1, \dots, 5$) in terms of the SCNI method can be described by

$$\tilde{u}_{j,k}^h(\mathbf{x}_K) = \frac{1}{A_K} \int_{\Omega_K} u_{j,k}^h(\mathbf{x}) d\Omega = \sum_{I=1}^{NP} b_{Ik}(\mathbf{x}_K) u_{jI}, \quad k = \{1, 2\}, \quad (11)$$

where $\tilde{u}_{j,k}^h(\mathbf{x}_K)$ is the derivatives for the x_k -axis ($k=1, 2$) and A_K is the area of Ω_K . $(\tilde{})$ represents the smoothed physical quantities in Ω_K . The scalar value $b_{Ik}(\mathbf{x}_K)$ is calculated by a line integral as:

$$b_{Ik}(\mathbf{x}_K) = \frac{1}{A_K} \int_{\Gamma_K} \psi_I(\mathbf{x}) n_k d\Gamma, \quad k = \{1, 2\}. \quad (12)$$

n_k denotes the x_k -components of the normal vector. The physical values of each node are evaluated.

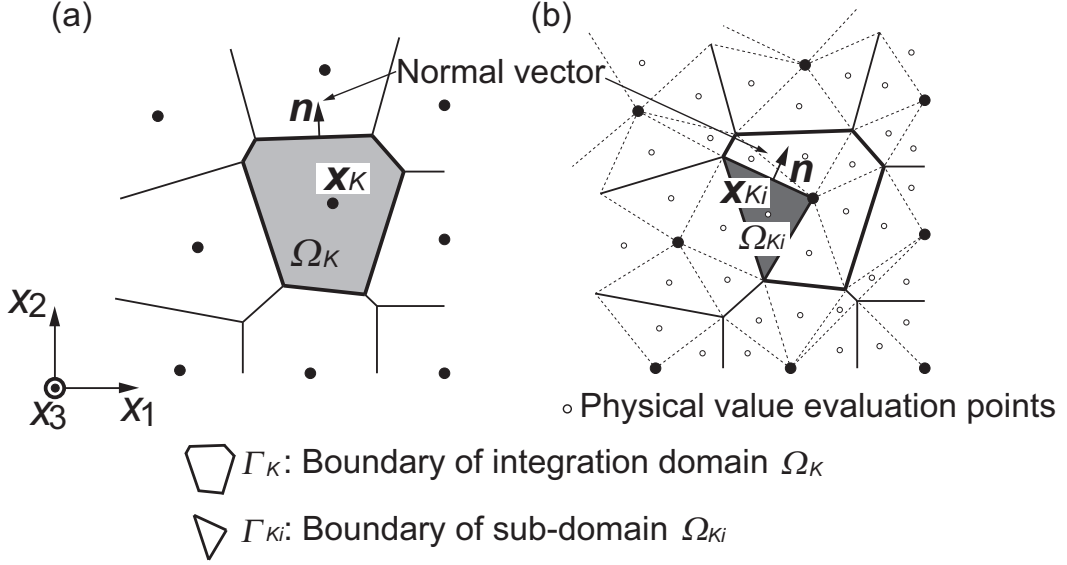


Figure 3: A schematic illustration of the nodal integration techniques: (a) SCNI, (b) SSCI.

When analyzing the linear buckling problems employing the meshfree flat shell formulation, an improved nodal integration technique is needed to accurately integrate the stiffness matrices, as well as the fracture modeling in [29,30]. SSCI is introduced. The area of SCNI Ω_K is further divided into a number of triangular areas (sub-domains) Ω_{K_i} as shown in Fig.3(b). And, SCNI is adopted for each sub-domains. The physical values are evaluated at the gravity center \mathbf{x}_{K_i} . The differentiations $\tilde{u}_{j,k}^h(\mathbf{x}_{K_i})$ of the components $\tilde{u}_j^h(\mathbf{x}_{K_i})$ are expressed as:

$$\tilde{u}_{j,k}^h(\mathbf{x}_{K_i}) = \frac{1}{A_{K_i}} \int_{\Omega_{K_i}} u_{j,k}^h(\mathbf{x}) d\Omega = \sum_{I=1}^{NP} b_{Ik}(\mathbf{x}_{K_i}) u_{jI}, \quad k = \{1, 2\}, \quad (13)$$

where the scalar value $b_{Ik}(\mathbf{x}_{K_i})$ is defined by

$$b_{Ik}(\mathbf{x}_{K_i}) = \frac{1}{A_{K_i}} \int_{\Gamma_{K_i}} \psi_I(\mathbf{x}) n_k d\Gamma, \quad k = \{1, 2\}. \quad (14)$$

A_{K_i} is the area of Ω_{K_i} , n_k is the normal vector components \mathbf{n} along the boundary of the sub-domains Γ_{K_i} . When evaluating a line integration in Eqs.(12) and (14), a 5-point Gauss quadrature rule is adopted.

When analyzing the flat shell formulation including the shear deformation, rotational components are included in the shear strain term. These components $\tilde{u}_j^h(\mathbf{x}_K)$ are numerically integrated by a surface integral as:

$$\tilde{u}_j^h(\mathbf{x}_K) = \frac{1}{A_K} \int_{\Omega_K} u_j^h(\mathbf{x}) d\Omega = \sum_{I=1}^{NP} b_I(\mathbf{x}_K) u_{jI}. \quad (15)$$

The scalar value $b_I(\mathbf{x}_K)$ is evaluated by dividing the Voronoi cell into a number of triangular sub-domains, as:

$$b_I(\mathbf{x}_K) = \frac{1}{A_K} \sum_{i=1}^{NC} \int_{\Omega_{K_i}} \psi_I d\Omega, \quad (16)$$

where NC is a number of triangles in a Voronoi cell. A 13-point Gauss quadrature rule is applied to the surface integral of each triangle. In solving in Eq.(2), a 3-point Newton-Cotes integration is employed to numerically integrate along the plate thickness direction.

2.2.2. Discrete equation

A linear equation is derived by considering the strain tensor $\boldsymbol{\varepsilon}_L$ in Eq.(3) and the displacement vector in Eq.(7). The displacement-strain relationship is expressed as

$$\{\varepsilon_{L11} \ \varepsilon_{L22} \ 2\varepsilon_{L12} \ 2\varepsilon_{L31} \ 2\varepsilon_{L23}\}^T = \sum_{I=1}^{NP} \mathbf{B}_{LI} \mathbf{U}_I, \quad (17)$$

where \mathbf{B}_{LI} and \mathbf{U}_I respectively are the displacement-strain matrix and the coefficient vector:

$$\mathbf{B}_{LI} = \begin{bmatrix} b_{I1} & 0 & 0 & 0 & zb_{I1} & 0 \\ 0 & b_{I2} & 0 & -zb_{I2} & 0 & 0 \\ b_{I2} & b_{I1} & 0 & -zb_{I1} & zb_{I2} & 0 \\ 0 & 0 & b_{I1} & 0 & b_I & 0 \\ 0 & 0 & b_{I2} & -b_I & 0 & 0 \end{bmatrix}, \quad (18)$$

$$\mathbf{U}_I = \{u_{1I} \ u_{2I} \ u_{3I} \ u_{4I} \ u_{5I} \ u_{6I}\}^T, \quad (19)$$

in which b_{Ik} ($k=1, 2$) is a line integral in Eqs.(12) and (14), and b_I is a surface integral in Eq.(16).

The detail of the nonlinear strain $\boldsymbol{\varepsilon}_{NL}$ is presented here. For convenience in the representation, a vector \mathbf{d}^h is defined as:

$$\mathbf{d}^h = \left\{ \frac{\partial u_1^h}{\partial x_1} \frac{\partial u_2^h}{\partial x_1} \frac{\partial u_3^h}{\partial x_1} \frac{\partial u_1^h}{\partial x_2} \frac{\partial u_2^h}{\partial x_2} \frac{\partial u_3^h}{\partial x_2} \frac{\partial u_1^h}{\partial x_3} \frac{\partial u_2^h}{\partial x_3} \frac{\partial u_3^h}{\partial x_3} \right\}^T. \quad (20)$$

By substituting Eq.(7) into Eq.(20), following relationship is obtained:

$$\mathbf{d}^h = \sum_{I=1}^{NP} \mathbf{B}_{NLI} \mathbf{U}_I, \quad (21)$$

where \mathbf{B}_{NLI} is a matrix constituted by b_{Ik} ($k=1, 2$) and b_I as:

$$\mathbf{B}_{NLI} = \begin{bmatrix} b_{I1} & 0 & 0 & 0 & zb_{I1} & 0 \\ 0 & b_{I1} & 0 & -zb_{I1} & 0 & 0 \\ 0 & 0 & b_{I1} & 0 & 0 & 0 \\ b_{I2} & 0 & 0 & 0 & zb_{I2} & 0 \\ 0 & b_{I2} & 0 & -zb_{I2} & 0 & 0 \\ 0 & 0 & b_{I2} & 0 & 0 & 0 \\ 0 & 0 & 0 & 0 & b_I & 0 \\ 0 & 0 & 0 & -b_I & 0 & 0 \\ 0 & 0 & 0 & 0 & 0 & 0 \end{bmatrix}. \quad (22)$$

Substituting Eqs.(18) and (22) into Eq.(2), a discrete equation of the eigenvalue problem is obtained as:

$$(\mathbf{K}_L + \lambda \mathbf{K}_{NL}) \mathbf{U} = 0, \quad (23)$$

where λ is the buckling coefficient, \mathbf{K}_L is the linear stiffness and \mathbf{K}_{NL} is the nonlinear stiffness matrix. Their details are given by

$$\mathbf{K}_{L\ IJ} = \sum_{K=1}^{NP} \mathbf{B}_{L\ I}^T(\mathbf{x}_K) \mathbf{D} \mathbf{B}_{L\ J}(\mathbf{x}_K) A_K, \quad (24)$$

$$\mathbf{K}_{NL\ IJ} = \sum_{K=1}^{NP} \mathbf{B}_{NL\ I}^T(\mathbf{x}_K) \boldsymbol{\sigma}'_0(\mathbf{x}_K) \mathbf{B}_{NL\ J}(\mathbf{x}_K) A_K. \quad (25)$$

2.2.3. Introducing the drilling rotation component

A flat shell formulation, which involves 5DOFs per node, has previously developed and detailed in [45]. However, there are difficulties in the modeling

of assembled structure geometries by the 5DOF formulation and discretization. Therefore, an in-plane rotation component θ_3 is introduced into the present formulation. Based on the idea of Kanok [47], the 6th DOF is introduced.

A penalty energy is defined by

$$W_T = \kappa_T G t_h A_K \left[\theta_3 - \frac{1}{2} \left(\frac{\partial u_{2mid}}{\partial x_1} - \frac{\partial u_{1mid}}{\partial x_2} \right) \right]^2, \quad (26)$$

where G is a shear modulus while κ_T is a parameter to determine amount of penalty energy. Kanok [47] recommended more than 0.1 to suppress a spurious torsional mode. It is noted that the penalty energy becomes zero for a rigid body rotation. The virtual strain e_{θ_3} related in-plane rotation θ_3 is then expressed as follows:

$$e_{\theta_3} = \theta_3 - \frac{1}{2} \left(\frac{\partial u_{2mid}}{\partial x_1} - \frac{\partial u_{1mid}}{\partial x_2} \right). \quad (27)$$

When the virtual stress is defined as $R_{\theta_3} = 2\kappa_T G e_{\theta_3}$, Eq.(26) can be rewritten as:

$$W_T = \frac{1}{2} \kappa_T R_{\theta_3} e_{\theta_3} t_h A_K. \quad (28)$$

The penalty energy is added to Eq.(2) as a virtual energy δW_T due to virtual strain δe_{θ_3} as:

$$\int_V \boldsymbol{\sigma} : \delta \boldsymbol{\varepsilon}_L dV + \delta W_T + \lambda \int_V \boldsymbol{\sigma}'_0 : \delta \boldsymbol{\varepsilon}_{NL} dV = 0. \quad (29)$$

e_{θ_3} is discretized by the RKs as:

$$e_{\theta_3} = \sum_{I=1}^{NP} \left\{ \frac{1}{2} b_{I2} \quad - \frac{1}{2} b_{I1} \quad 0 \quad 0 \quad 0 \quad b_I \right\} = \sum_{I=1}^{NP} \mathbf{B}_{\theta_3 I} \mathbf{U}_I. \quad (30)$$

Therefore, the linear stiffness matrix \mathbf{K}_L in Eq.(24) is rewritten as:

$$\mathbf{K}_{L IJ} = \sum_{K=1}^{NP} \mathbf{B}_{L I}^T(\mathbf{x}_K) \mathbf{D} \mathbf{B}_{L J}(\mathbf{x}_K) A_K + \sum_{K=1}^{NP} \mathbf{B}_{\theta_3 I}^T(\mathbf{x}_K) \alpha_K \mathbf{B}_{\theta_3 J}(\mathbf{x}_K), \quad (31)$$

where the second term of the right-hand side of Eq.(31) is obtained by discretizing δW_T and $\alpha_K = 2\kappa_T G t_h A_K$.

3. Meshfree modeling of stiffened plate structures

In dealing with the assembled plate structures in the finite element (FE) modeling, duplicate nodes along the joints are merged to equalize the physical values. The meshfree modeling can thus be achieved by introducing the SKs, as well as the finite element method (FEM). The meshfree modeling of assembled structures is briefly explained.

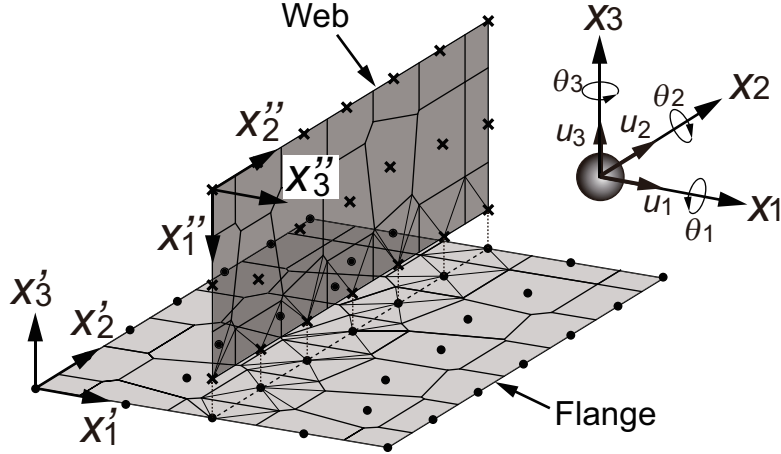


Figure 4: Modeling of T-shaped plate structure.

Meshfree discretization and modeling of a T-shaped structure is schematically illustrated in Fig.4. The web is attached vertically to the flange. The web/flange are arranged independently. The global coordinate system of the T-shaped structure is x_1 - x_2 - x_3 . The unit vector is \mathbf{e} . And, the displacement and solution vectors are \mathbf{u}^h and \mathbf{U} . The local coordinate system and physical values for the flange and web are represented $(\)'$ and $(\)''$, respectively. For example, the unit vectors \mathbf{e}' and \mathbf{e}'' for the flange and web can be written, as:

$$\mathbf{e}' = \begin{bmatrix} 1 & 0 & 0 \\ 0 & 1 & 0 \\ 0 & 0 & 1 \end{bmatrix}, \quad \mathbf{e}'' = \begin{bmatrix} 0 & 0 & -1 \\ 0 & 1 & 0 \\ 1 & 0 & 0 \end{bmatrix}. \quad (32)$$

The relationships between the global and local coordinate systems are rep-

resented, for \mathbf{u}^h and \mathbf{U} , as:

$$\mathbf{u}^h = \begin{bmatrix} \mathbf{T}' & \mathbf{0} \\ \mathbf{0} & \mathbf{T}'' \end{bmatrix}^T \begin{Bmatrix} \mathbf{u}^{h'} \\ \mathbf{u}^{h''} \end{Bmatrix}, \quad (33)$$

$$\mathbf{U} = \begin{bmatrix} \mathbf{T}' & \mathbf{0} \\ \mathbf{0} & \mathbf{T}'' \end{bmatrix}^T \begin{Bmatrix} \mathbf{U}' \\ \mathbf{U}'' \end{Bmatrix}, \quad (34)$$

where \mathbf{T}' and \mathbf{T}'' are the transformation matrices. They are written employing the unit vectors \mathbf{e}' and \mathbf{e}'' , as:

$$\mathbf{T}' = \begin{bmatrix} \mathbf{e}' & \mathbf{0} & \cdots & \mathbf{0} & \mathbf{0} \\ \mathbf{0} & \mathbf{e}' & \cdots & \mathbf{0} & \mathbf{0} \\ \vdots & \vdots & \ddots & \vdots & \vdots \\ \mathbf{0} & \mathbf{0} & \cdots & \mathbf{e}' & \mathbf{0} \\ \mathbf{0} & \mathbf{0} & \cdots & \mathbf{0} & \mathbf{e}' \end{bmatrix}, \quad \mathbf{T}'' = \begin{bmatrix} \mathbf{e}'' & \mathbf{0} & \cdots & \mathbf{0} & \mathbf{0} \\ \mathbf{0} & \mathbf{e}'' & \cdots & \mathbf{0} & \mathbf{0} \\ \vdots & \vdots & \ddots & \vdots & \vdots \\ \mathbf{0} & \mathbf{0} & \cdots & \mathbf{e}'' & \mathbf{0} \\ \mathbf{0} & \mathbf{0} & \cdots & \mathbf{0} & \mathbf{e}'' \end{bmatrix}. \quad (35)$$

Therefore, the stiffness matrices \mathbf{K}_L and \mathbf{K}_{NL} in the global coordinate system can be represented as:

$$\begin{aligned} \mathbf{K}_L &= \begin{bmatrix} \mathbf{T}' & \mathbf{0} \\ \mathbf{0} & \mathbf{T}'' \end{bmatrix}^T \begin{bmatrix} \mathbf{K}'_L & \mathbf{0} \\ \mathbf{0} & \mathbf{K}''_L \end{bmatrix} \begin{bmatrix} \mathbf{T}' & \mathbf{0} \\ \mathbf{0} & \mathbf{T}'' \end{bmatrix}, \\ \mathbf{K}_{NL} &= \begin{bmatrix} \mathbf{T}' & \mathbf{0} \\ \mathbf{0} & \mathbf{T}'' \end{bmatrix}^T \begin{bmatrix} \mathbf{K}'_{NL} & \mathbf{0} \\ \mathbf{0} & \mathbf{K}''_{NL} \end{bmatrix} \begin{bmatrix} \mathbf{T}' & \mathbf{0} \\ \mathbf{0} & \mathbf{T}'' \end{bmatrix}. \end{aligned} \quad (36)$$

4. Numerical examples

Several numerical examples for the linear buckling problems of stiffened plate structures are presented. The coefficient of the penalty energy in Eq.(26) is set $\kappa_T=0.1$. The Young's modulus $E=205.8$ GPa and the Poisson's ratio $\nu=0.3$ are taken throughout the study.

4.1. Perforated plates

The main purpose of this section is to verify the accuracy of our improved meshfree flat shell model with 6DOFs. The calculated results are hence compared with that derived from the formulation using 5DOFs [45]. By doing so, calculation is started with perforated plates assuming several boundary and loading conditions. The size of the rectangular plate is shown in Fig.5(a). The plate thickness t_h is 12 mm. The plate length is a and the breadth is

b. Two kinds of plate sizes are chosen. One is $a=1,600$ mm and $b=800$ mm, and the other is $a=2,400$ mm and $b=800$ mm, respectively. The aspect ratios a/b are 2.0 and 3.0. The opening ratio d/b varies from 0.1 to 0.8. Three kinds of loading conditions as sketched in Fig.5(a) are considered. They are longitudinal thrust σ_{11} , transverse thrust σ_{22} and shear stress τ_{12} . All edges are kept straight and a simply supported condition is assumed. Then longitudinal/transverse/shear stress is applied. When shear stress τ_{12} is adopted, the boundary conditions in Fig.5(b) are employed. A meshfree model for a perforated plate is shown in Fig.5(c). A close-up view of the model is also given.

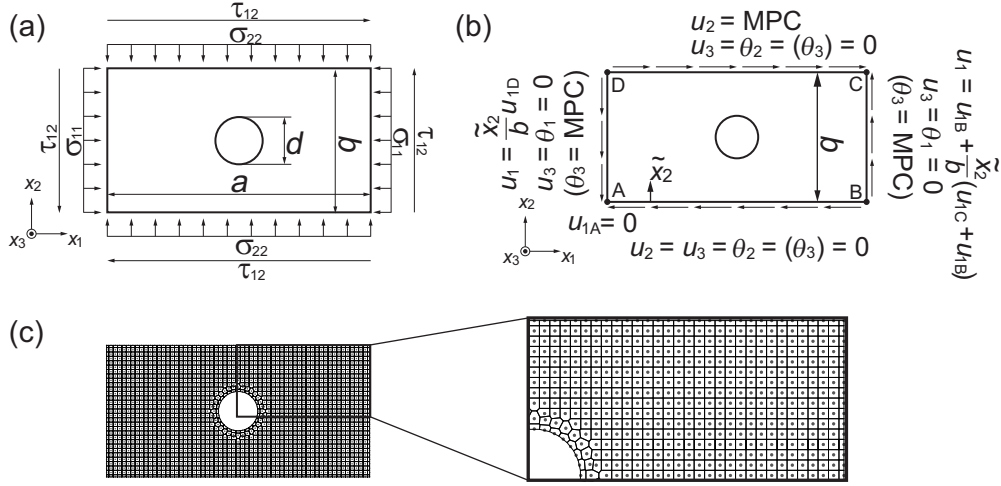


Figure 5: Meshfree modeling of a perforated plate: (a) loading conditions, (b) boundary conditions under shear stress τ_{12} , (c) a meshfree model for $a/b=2.0$ and $d/b=0.3$.

The scattered nodes are uniformly distributed throughout the entire analysis domain, and 31 nodes are used along the breadth b . Voronoi cell is adopted for generating the meshfree model and the nodal integration. SCNI is only employed for the nodal integration of the stiffness matrix. The numerical results are compared with the formulas in [67]. The formulas are also presented in Appendix 1. Here, we define a perforation factor R , as:

$$R = \sigma_{cr.}/\sigma_{cr0.}, \quad (37)$$

where $\sigma_{cr.}$ and $\sigma_{cr0.}$ are critical buckling stresses with and without openings.

Buckling loads/modes under longitudinal thrust are examined. The results for $a/b=2.0$ are shown in Fig.6(a). Two lines are by the formulas

[67], while the symbols are the meshfree results. 'm' represents the buckling half-wave number. When $m=2$, the perforation factor R_{11} increases as d/b increases. On the other hand, the perforation factor R_{11} decreases with increasing d/b . In this case, m varies from 3 to 1. Therefore, two half-waves buckling mode can be obtained when d/b is less than 0.22, and one half-wave buckling mode is obtained for more than $d/b=0.22$ as the first order buckling mode. The results for $a/b=3.0$ are presented in Fig.6(b). Three half-waves buckling mode is obtained for all d/b . The perforation factor R_{11} decreases when d/b is less than 0.6, but it increases if d/b is greater than 0.6. The 5DOFs and 6DOFs results for both cases are found very close.

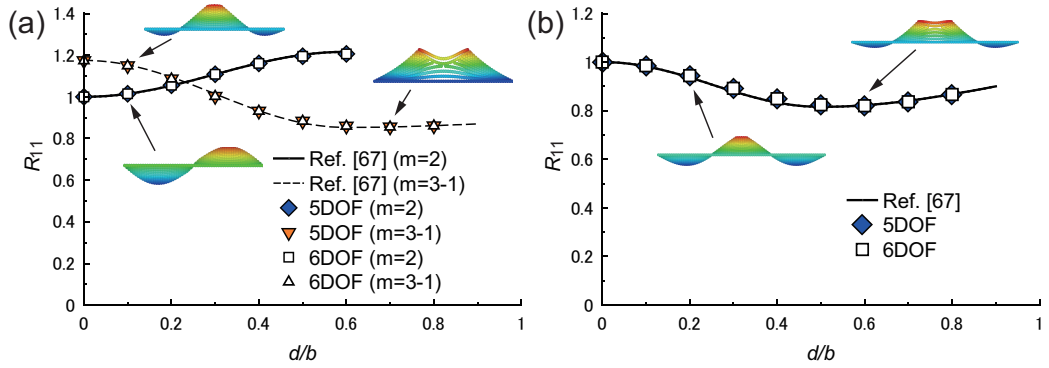


Figure 6: Perforation factor for d/b under longitudinal thrust: (a) $a/b=2.0$, (b) $a/b=3.0$.

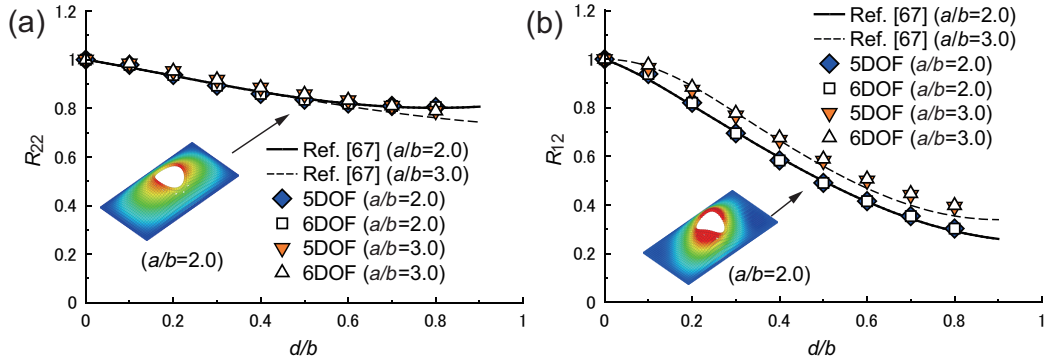


Figure 7: Perforation factor for d/b under transverse thrust and shear stress: (a) transverse thrust, (b) shear stress.

The calculated buckling stresses under transverse thrust are shown in Fig.7(a) for $a/b=2.0$ and 3.0 , respectively. One half-wave buckling mode can

be seen both for $a/b=2.0$ and 3.0 . The perforation factor R_{22} decreases with increasing d/b . In addition, the calculated shear buckling stress are shown in Fig.7(b) for $a/b=2.0$ and 3.0 . A similar tendency to the R_{22} is found for the perforation factor R_{12} . The 6DOFs meshfree results in Figs.7(a) and (b) are consistent. The same perforated plates are analyzed imposing several different boundary conditions, and it is found that the 6DOFs meshfree formulation and discretization is effective.

4.2. T-shaped structure

The web/flange modeling and adoption of the nodal integration technique are critically examined by analyzing stiffened members. Linear buckling analysis of a T-shaped structure is carried out. The geometry and boundary/loading conditions are represented in Fig.8(a). The lengths of the flange are $a=500, 1,000, 1,500$ mm respectively, and the breadth of the flange $b=500$ mm. Therefore, aspect ratios of the flange are $a/b=1.0, 2.0, 3.0$, respectively. The web height is $b/2$. The cross-section of the T-shaped structure is depicted in Fig.8(b). The plate thickness of the flange and the web are assumed $0.02b$ and $0.04b$ to examine accuracy of the modeling. Longitudinal thrust is applied. Both cross-sections of the structure are clamped except in the x_1 -direction, and the other two edges are simply supported.

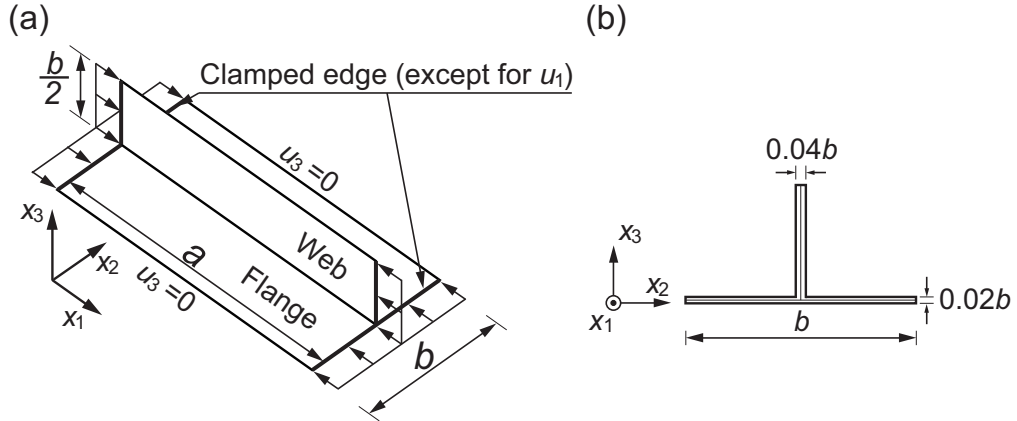


Figure 8: A T-shaped structure: (a) loading and boundary conditions, (b) cross-section.

Two kinds of meshfree modeling are chosen. One is the full SCNI model and the other is the SCNI/SSCI hybrid model. They are presented in Figs.9(a) and (b), respectively. The node spacing is $\alpha=b/14$ mm. SSCI

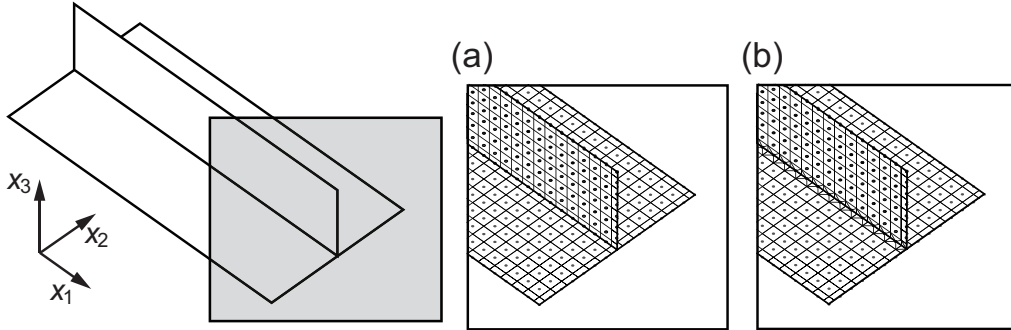


Figure 9: Node distributions and domain/sub-domain for the nodal integration ($\alpha=b/14$ mm): (a) full SCNI model, (b) SCNI/SSCI hybrid model.

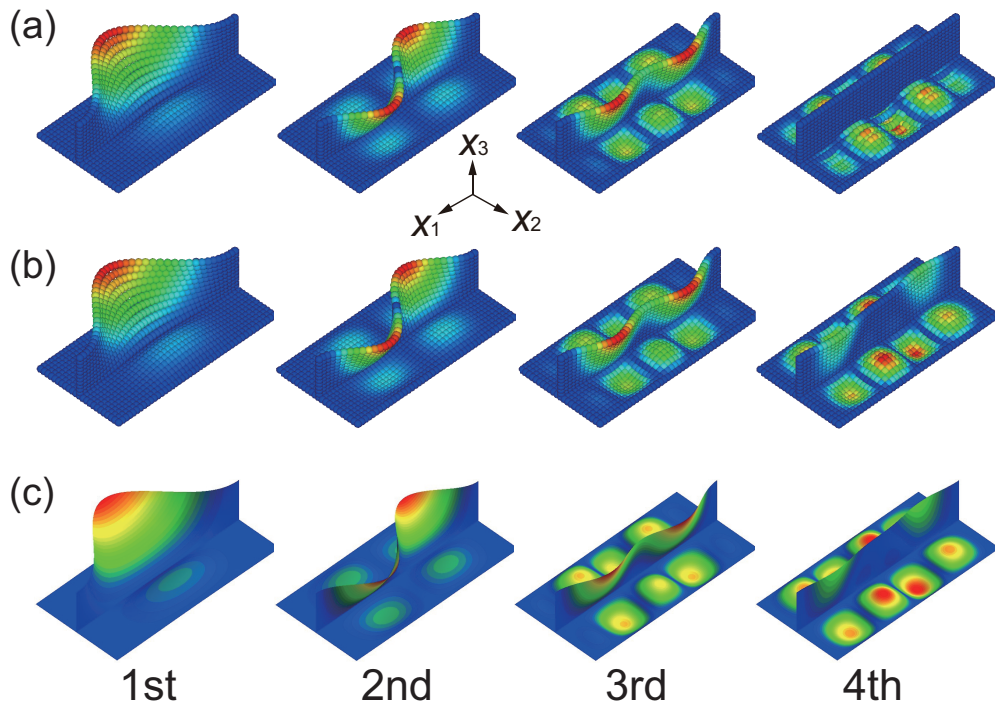


Figure 10: Comparisons of the first four buckling modes for the T-shaped structure ($a/b=2.0$): (a) full SCNI model, (b) SCNI/SSCI hybrid model, (c) FEM.

is adopted along the web/flange connection in the hybrid model. For the comparison purpose, other numerical solutions derived from the commercial FEM software (MSC.Marc) using 4-node thick quadrilateral shell element (the element number: 75) are added. The first four buckling modes for $a/b=2.0$ are presented in Figs.10(a), (b) and (c) which correspond to the full SCNI, SCNI/SSCI hybrid and FE models, respectively. The present numerical results of buckling modes by three different models show a very good agreement for the first three modes. The hybrid SCNI/SSCI model works perfectly, although the fourth buckling mode is a little different from that of the full SCNI model. The calculated buckling stress for $a/b=2.0$ is also presented in Table 1. Fine meshfree model $\alpha=b/22$ mm is employed.

Table 1: Comparison of the first four buckling stresses σ_{cr} for the T-shaped structure ($\alpha=b/22$ mm) among the full SCNI, hybrid SCNI/SSCI and the FEM.

[KN/mm ²]	1st	2nd	3rd	4th
SCNI	1.036	1.135	1.517	1.531
HYBRID	1.034	1.137	1.517	1.546
FEM	1.034	1.137	1.519	1.549

The first four buckling stresses calculated by the hybrid model are in good agreement with the reference solutions. The convergence study with the hybrid models is carried out for $a/b=1.0$, 2.0 and 3.0, respectively. Five kinds of node spacings $\alpha=b/10$, $b/12$, $b/14$, $b/16$, and $b/18$ mm are adopted. The error η (%) is defined as:

$$\eta (\%) = \left| \frac{\sigma_{cr.} - \sigma_{ref.}}{\sigma_{ref.}} \right| \times 100, \quad (38)$$

where $\sigma_{cr.}$ is the first order buckling stress evaluated by the meshfree model, and $\sigma_{ref.}$ is the reference solution. The results are shown in Fig.11. They are monotonously converged as the node density increased for all aspect ratios.

The SCNI operation smoothens the stress/strain within the Voronoi cell. On the other hand, stress concentration is sometimes generated around the web/flange connections. Therefore, the accuracy of the buckling loads/modes decreases in the higher order buckling modes when only the SCNI is adopted. Because the stress/strain evaluation is improved by the SSCI with the triangular domains along the joints, the hybrid model can represent buckling loads/modes well. Similar results can be found for 5DOFs meshfree formulation and discretization in [45].

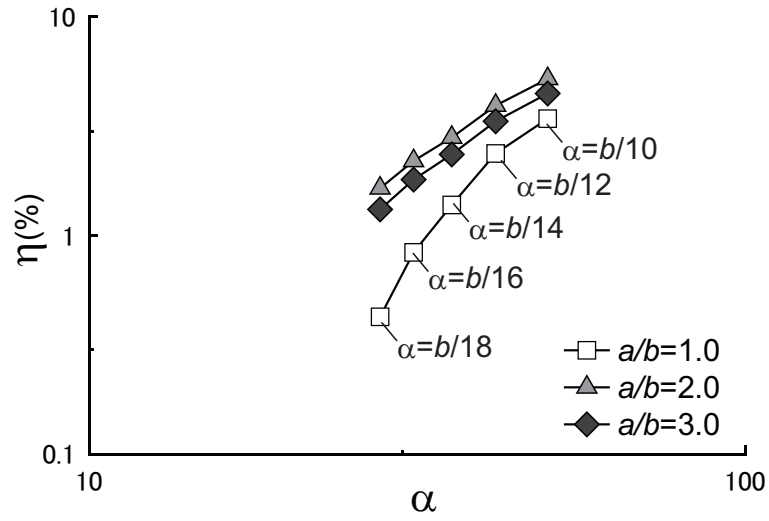


Figure 11: Convergence study for T-shaped structures.

4.3. Stiffened plate structure in ship structure

The buckling modes/loads of stiffened plate structures in ships are examined to verify the effectiveness of the present meshfree formulation and discretization. Two types of stiffeners, *i.e.*, flat-bar and angle-bar are assumed. The geometries and parameters are shown in Figs.12(a) and (b), and dimensions of the stiffeners are presented in Table 2. The stiffened plate structures were analyzed in [4,9].

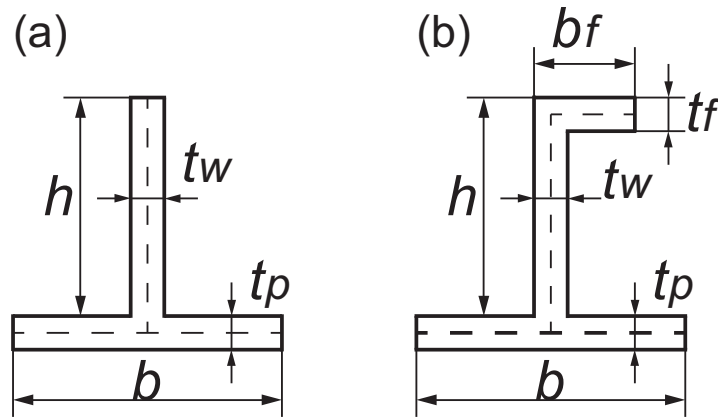


Figure 12: Cross-section of stiffeners: (a) flat-bar, (b) angle-bar.

Table 2: Dimensions of the stiffeners.

Flat-bar	Angle-bar
$h \times t_w$	$h \times b_f \times t_w/t_f$
550×35	$600 \times 150 \times 15/20$

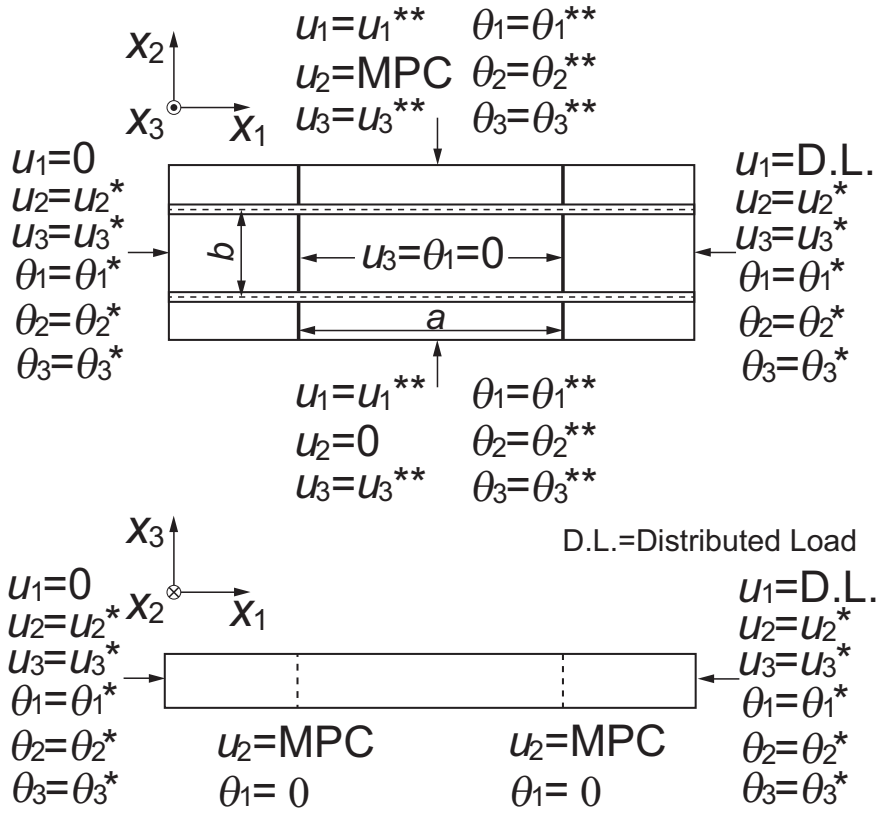


Figure 13: Model size and boundary conditions for the continuous stiffened plate model.

Linear buckling analyses are carried out for the stiffened plate structures. The dimensions and the boundary conditions employed in this study are shown in Fig.13. The aspect ratio a/b is 3.0 ($a=2,550$ mm, $b=850$ mm). By assuming continuity of the structures, a continuous stiffened plate model is employed. The triple-span triple-bay model is adopted and a periodical boundary condition is imposed. As a loading condition, uniaxial thrust is applied in x_1 -direction. Here, slenderness ratio of the plate is defined by the following equation.

$$\beta = \frac{b}{t_p} \sqrt{\frac{\sigma_Y}{E}}, \quad (39)$$

where σ_Y is yield stress. $\sigma_Y=313.6$ MPa is assumed. The plate thickness $t_p=33, 22, 16, 13, 11,$ and 9.5 mm are employed for the flat-bar and angle-bar models. Therefore, $\beta=1.01, 1.51, 2.07, 2.55, 3.02$ and 3.49 , respectively. The meshfree models for the plate with the flat-bar and angle-bar stiffeners are respectively presented in Figs.14(a) and (b). The scattered nodes are uniformly distributed on the flat-bar and angle-bar models. The node spacing is $\alpha=b/16$. The web/flange connections are divided in triangular domains, and SSCI is employed. The buckling loads/modes are examined. A very fine FEM model is adopted as the reference solutions.

The numerical results of the flat-bar and angle-bar models are respectively shown in Figs.15(a) and (b). The vertical axis is buckling stress normalized by σ_Y . The horizontal axis is β . As β increases, the normalized buckling stress decreases. The results with the meshfree modeling show a good agreement with the reference solutions. The buckling modes of the flat-bar and angle-bar are visualized in Fig.16 and 17 for $\beta=1.01, 2.07$ and 2.55 , respectively. For the case of the flat-bar model with $\beta=1.01$, the plate is very thick and stiffer buckles. As the plate becomes thinner, both plate and stiffener buckle, for example when $\beta=2.07$. For more thinner plate, only plate buckles. For the angle-bar model, global buckling of the stiffeners does not appear because the flexural rigidity is high compared with that of the flat-bar model. When $\beta=1.01$, local buckling could be seen in the web of the angle bar. Three half-waves buckling mode could be seen in the plate when $\beta=2.07$. The four half-waves buckling mode is generated in the plate of $\beta=2.55$ because resistance of the stiffener against the local plate deflection increases. In all the cases, the buckling modes of the meshfree models are in good agreement with the reference solutions.

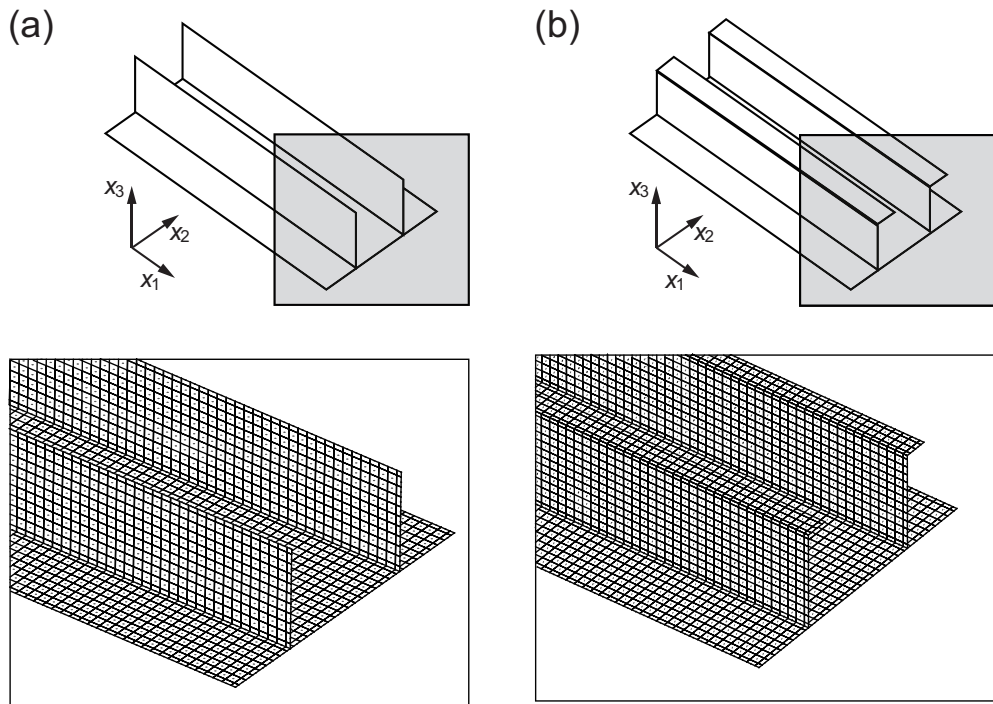


Figure 14: Meshfree models for stiffened plate structures: (a) flat-bar model, (b) angle-bar model.

5. Conclusion

All the desirable characteristics of the proposed meshfree formulation are demonstrated through several numerical examples including perforated plates and stiffened plates with different configurations, loading and boundary conditions. The present numerical results calculated by the proposed approaches are compared with the reference solutions obtained by the FEM. It is indicated that the present meshfree formulations are effective in modeling buckling of perforated and stiffened plate structures.

Acknowledgements

The authors would like to express our gratitude to Ken-ichiro Yoshida (Graduate School of Engineering, Hiroshima University) for giving us valuable comments on this research. This research was partially supported by the JSPS Grants-in-Aid for Scientific Research (A)(15H02328) and (C)(15K06632).

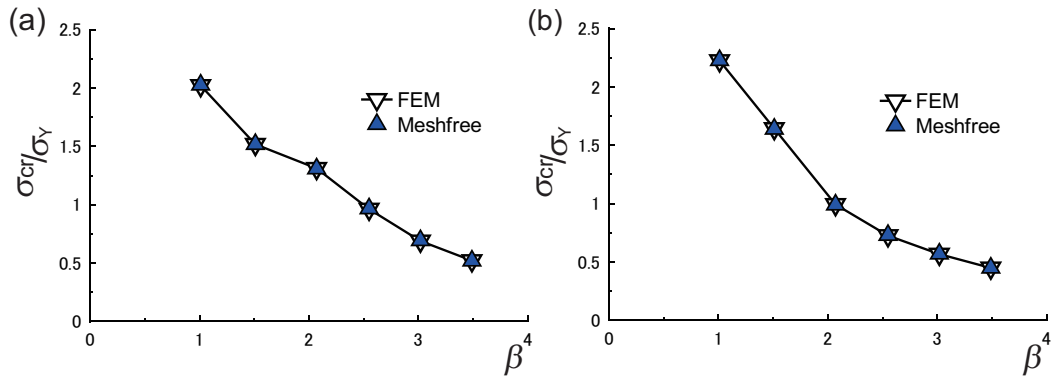


Figure 15: Buckling strength of stiffened plate: (a) flat-bar model, (b) angle-bar model.

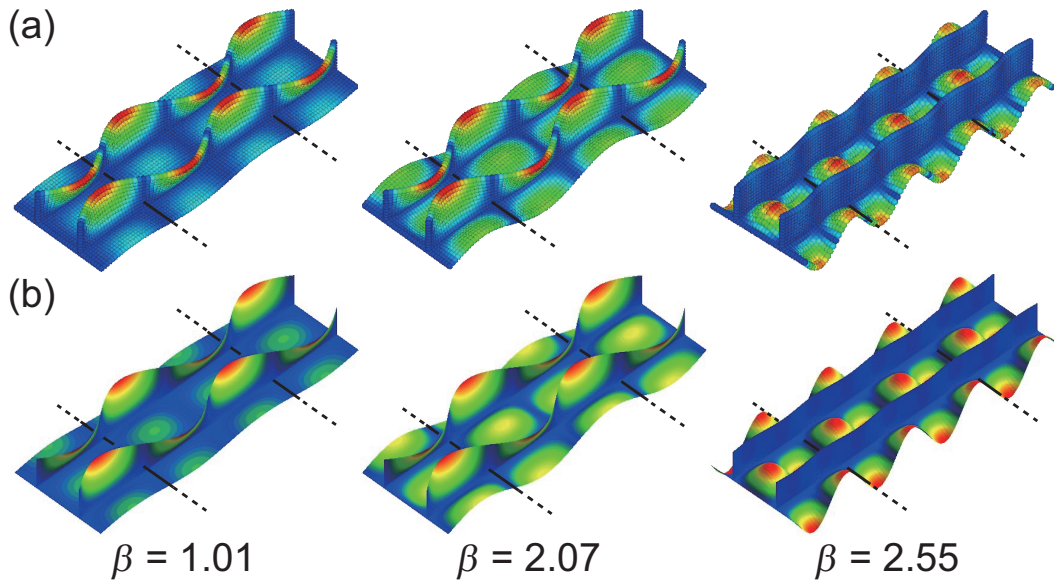


Figure 16: Buckling modes of flat-bar: (a) meshfree, (b) FEM.

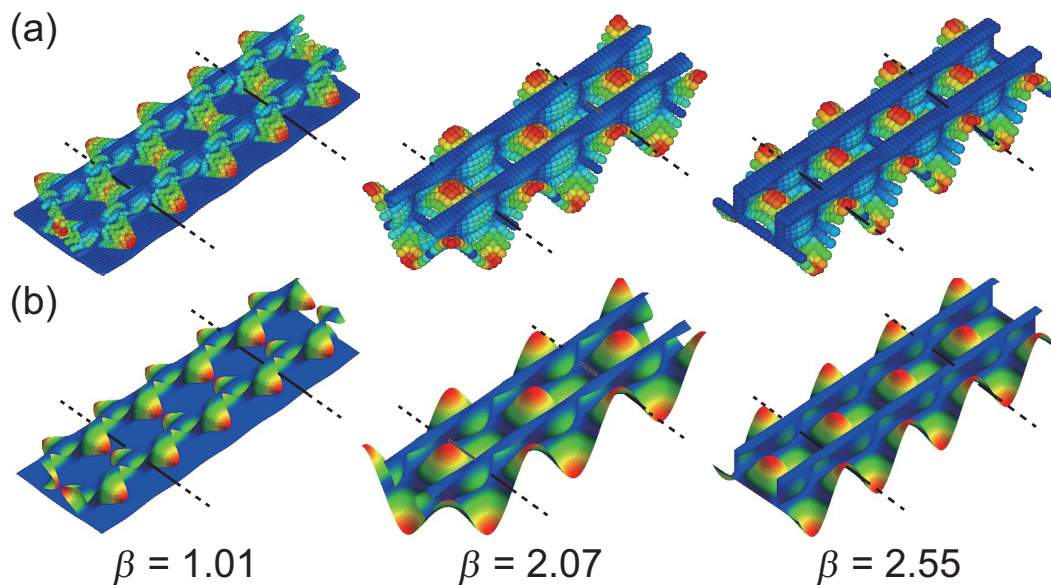


Figure 17: Buckling modes of angle-bar: (a) meshfree, (b) FEM.

This work was performed as a part of the Cooperative Research Program of the Joining and Welding Research Institute, Osaka University. Tinh Quoc Bui gratefully acknowledges the support from Grant-in-Aid for Scientific Research - JSPS.

References

- [1] T. Yao, O.C. Astrup, P. Caridis, Y.N. Chen, S.R. Cho, R.S. Dow, O. Niho, P. Rigo, Ultimate hull girder strength, Proceedings of the 14th International Ship and Offshore Structures Congress (ISSC) (2000) 321-391.
- [2] T. Yao, Hull girder strength, Mar. Struct. 16 (2003) 1-13.
- [3] T. Yao, P.I. Nikolov, Progressive collapse analysis of a ship's hull under longitudinal bending, J. Soc. Nav. Arch. Jpn. 170 (1991) 449-461.
- [4] Report of research committee for verification of ISO formulas to evaluate ultimate strength, The Japan Society of Naval Architects and Ocean Engineers. (2011).

- [5] M. Fujikubo, T. Yao, M.R. Khedmati, M. Harada, D. Yanagihara, Estimation of ultimate strength of continuous stiffened panel under combined transverse thrust and lateral pressure Part 1: Continuous plate, *Mar. Struct.* 18 (2005) 383-410.
- [6] M. Fujikubo, M. Harada, T. Yao, M.R. Khedmati, D. Yanagihara, Estimation of ultimate strength of continuous stiffened panel under combined transverse thrust and lateral pressure Part 2: Continuous stiffened panel, *Mar. Struct.* 18 (2005) 411-427.
- [7] M.C. Xu, D. Yanagihara, M. Fujikubo, C.G. Soares, Influence of boundary conditions on the collapse behaviour of stiffened panels under combined loads, *Mar. Struct.* 34 (2013) 205-225.
- [8] Z. Pei, K. Iijima, M. Fujikubo, Y. Tanaka, S. Tanaka, S. Okazawa, T. Yao, Collapse behaviour of a bulk carrier under alternate heavy loading condition, *Int. J. Offshore Polar Eng.* 23 (2013) 224-231.
- [9] S. Tanaka, D. Yanagihara, A. Yasuoka, M. Harada, S. Okazawa, M. Fujikubo, T. Yao, Evaluation of ultimate strength of stiffened panels under longitudinal thrust, *Mar. Struct.* 36 (2014) 21-50.
- [10] Z. Pei, K. Iijima, M. Fujikubo, S. Tanaka, S. Okazawa, T. Yao, Simulation on progressive collapse behaviour of whole ship model under extreme waves using idealized structural unit method, *Mar. Struct.* 40 (2015) 104-133.
- [11] T. Belytschko, Y.Y. Lu, L. Gu, Element-free Galerkin methods, *Int. J. Numer. Meth. Eng.* 37 (1994) 229-256.
- [12] W.K. Liu, S. Jun, Y.F. Zhang, Reproducing kernel particle methods, *Int. J. Numer. Meth. Fluid.* 20 (1995) 1081-1106.
- [13] X Zhang, T.Q Bui, A fictitious crack XFEM with two new solution algorithms for cohesive crack growth modeling in concrete structures, *Eng. Comput.* 32 (2015) 473-497.
- [14] P. Liu, T. Yu, T.Q Bui, Ch. Zhang, Transient dynamic crack analysis in non-homogeneous functionally graded piezoelectric materials by the X-FEM, *Comput. Mater. Sci.* 69 (2013) 542-558.

- [15] T.Q. Bui, S. Hirose, Ch. Zhang, T. Rabczuk, C.T. Wu, T. Saitoh, J. Lei, Extended isogeometric analysis for dynamic fracture in multiphase piezoelectric/piezomagnetic composites, *Mech. Mater.* 97 (2016) 135-163.
- [16] T.T. Yu, T.Q. Bui, S.H. Yin, D.H. Doan, C.T. Wu, T.V. Do, S. Tanaka, On the thermal buckling analysis of functionally graded plates with internal defects using extended isogeometric analysis, *Compos. Struct.* 136 (2016) 684-695.
- [17] T. Yu, S. Yin, T.Q. Bui, S. Xia, S. Tanaka, S. Hirose, NURBS-based isogeometric analysis of buckling and free vibration problems for laminated composites plates with complicated cutouts using a new simple FSDT theory and level set method, *Thin-Walled Struct.* 101 (2016) 141-156.
- [18] T.Q. Bui, Extended isogeometric dynamic and static fracture analysis for cracks in piezoelectric materials using NURBS, *Comput. Meth. Appl. Mech. Eng.* 295 (2015) 470-509.
- [19] S. Tanaka, H. Okada, S. Okazawa, A wavelet Galerkin method employing B-spline bases for solid mechanics problems without the use of a fictitious domain, *Comput. Mech.* 50 (2012) 35-48.
- [20] S. Tanaka, H. Okada, S. Okazawa, M. Fujikubo, Fracture mechanics analysis using the wavelet Galerkin method and extended finite element method, *Int. J. Numer. Meth. Eng.* 93 (2013) 1082-1108.
- [21] S. Tanaka, H. Suzuki, S. Ueda, S. Sannomaru, An extended wavelet Galerkin method with a high-order B-spline for 2D crack problems, *Acta Mech.* 226 (2015) 2159-2175.
- [22] S. Tanaka, S. Sannomaru, M. Imachi, S. Hagihara, S. Okazawa, H. Okada, Analysis of dynamic stress concentration problems employing spline-based wavelet Galerkin method, *Eng. Anal. Bound. Elem.* 58 (2015) 129-139.
- [23] S. Sannomaru, S. Tanaka, K. Yoshida, T.Q. Bui, S. Okazawa, S. Hagihara, Treatment of Dirichlet-type boundary conditions in the spline-based wavelet Galerkin method employing multiple point constraints, *Appl. Math. Model.* 43 (2017) 592-610.

- [24] P. Krysl, T. Belytschko, Analysis of thin plates by the element-free Galerkin method, *Comput. Mech.* 17 (1995) 26-35.
- [25] P. Krysl, T. Belytschko, Analysis of thin shells by the element-free Galerkin method, *Int. J. Solid. Struct.* 33 (1996) 3057-3080.
- [26] H. Noguchi, T. Kawashima, T. Miyamura, Element free analyses of shell and spatial structures, *Int. J. Numer. Meth. Eng.* 47 (2000) 1215-1240.
- [27] W. Kanok-Nukulchai, W. Barry, K. Saran-Yasoontorn, P.H. Bouillard, On elimination of shear locking in the element-free Galerkin method, *Int. J. Numer. Meth. Eng.* 52 (2001) 705-725.
- [28] Z. Zhang, H. Noguchi, J.S. Chen, Moving least-squares approximation with discontinuous derivative basis functions for shell structures with slope discontinuities, *Int. J. Numer. Meth. Eng.* 76 (2008) 1202-1230.
- [29] S. Tanaka, H. Suzuki, S. Sadamoto, M. Imachi, T.Q. Bui, Analysis of cracked shear deformable plates by an effective meshfree plate formulation, *Eng. Fract. Mech.* 144 (2015) 142-157.
- [30] S. Tanaka, H. Suzuki, S. Sadamoto, S. Sannomaru, T.T. Yu, T.Q. Bui, *J*-integral evaluation for 2D mixed-mode crack problems employing a meshfree stabilized conforming nodal integration method, *Comput. Mech.* 58 (2016) 185-198.
- [31] S. Tanaka, H. Suzuki, S. Sadamoto, S. Okazawa, T.T. Yu, T.Q. Bui, Accurate evaluation of mixed-mode intensity factors of cracked shear deformable plates by an enriched meshfree Galerkin formulation, *Arch. Appl. Mech.* 87 (2017) 279-298.
- [32] D. Organ, M. Fleming, T. Terry, T. Belytschko, Continuous meshless approximations for nonconvex bodies by diffraction and transparency, *Comput. Mech.* 18 (1996) 225-235.
- [33] P. Krysl, T. Belytschko, Element-free Galerkin method: Convergence of the continuous and discontinuous shape functions, *Comput. Meth. Appl. Mech. Eng.* 148 (1997) 257-277.
- [34] W.K. Liu, S. Jun, S. Li, J. Adee, T. Belytschko, Reproducing kernel particle methods for structural dynamics, *Int. J. Numer. Meth. Eng.* 38 (1995) 1655-1679.

- [35] J.S. Chen, C. Pan, C.T. Wu, W.K. Liu, Reproducing kernel particle methods for large deformation analysis of non-linear structures, *Comput. Meth. Appl. Mech. Eng.* 139 (1996) 195-227.
- [36] J.S. Chen, C. Pan, C.T. Wu, Large deformation analysis of rubber based on a reproducing kernel particle method, *Comput. Mech.* 19 (1997) 211-227.
- [37] D. Wang, P. Chen, Quasi-convex reproducing kernel meshfree method, *Comput. Mech.* 54 (2014) 689-709.
- [38] J.S. Chen, C.T. Wu, S. Yoon, Y. You, A stabilized conforming nodal integration for Galerkin meshfree methods, *Int. J. Numer. Meth. Eng.* 50 (2001) 435-466.
- [39] J.S. Chen, S. Yoon, C.T. Wu, Non-linear version of stabilized conforming nodal integration for Galerkin mesh-free methods, *Int. J. Numer. Meth. Eng.* 53 (2002) 2587-2615.
- [40] <http://www.qhull.org/> [accessed 10.6.16]
- [41] D. Wang, J.S. Chen, Locking-free stabilized conforming nodal integration for meshfree Mindlin-Reissner plate formulation, *Comput. Meth. Appl. Mech. Eng.* 193 (2004) 1065-1083.
- [42] D. Wang, J.S. Chen, A locking-free meshfree curved beam formulation with the stabilized conforming nodal integration, *Comput. Mech.* 39 (2006) 83-90.
- [43] D. Wang, Y. Sun, A Galerkin meshfree method with stabilized conforming nodal integration for geometrically nonlinear analysis of shear deformable plates, *Int. J. Comput. Meth.* 8 (2011) 685.
- [44] S. Sadamoto, S. Tanaka, S. Okazawa, Elastic large deflection analysis of plates subjected to uniaxial thrust using meshfree Mindlin-Reissner formulation, *Comput. Mech.* 52 (2013) 1313-1330.
- [45] K. Yoshida, S. Sadamoto, Y. Setoyama, S. Tanaka, T.Q. Bui, C. Murakami, D. Yanagihara, Meshfree flat-shell formulation for evaluating linear buckling loads and mode shapes of structural plates, *J. Mar. Sci. Tech.* 10.1007/s00773-017-0433-2.

- [46] S. Sadamoto, M. Ozdemir, S. Tanaka, K. Taniguchi, T.T. Yu, T.Q. Bui, An effective meshfree reproducing kernel method for buckling analysis of cylindrical shells with and without cutouts, *Comput. Mech.* 10.1007/s00466-017-1384-5.
- [47] W. Kanok-Nukulchai, A simple and efficient finite element for general shell analysis, *Int. J. Numer. Meth. Eng.* 14 (1979) 179-200.
- [48] S. Sadamoto, S. Tanaka, S. Okazawa, Modeling of plate structures for Galerkin meshfree methods (1st Report: modeling and linear analysis), *Trans. of JSME A* 79 (2013) 891-904. (in Japanese)
- [49] J.S. Chen, H.P. Wang, New boundary condition treatments in meshfree computation of contact problems, *Comput. Meth. Appl. Mech. Eng.* 187 (2000) 441-468.
- [50] D. Wang, J.S. Chen, A Hermite reproducing kernel approximation for thin-plate analysis with sub-domain stabilized conforming integration, *Int. J. Numer. Meth. Eng.* 74 (2008) 368-390.
- [51] D. Wang, Z. Lin, Free vibration analysis of thin plates using Hermite reproducing kernel Galerkin meshfree method with sub-domain stabilized conforming integration, *Comput. Mech.* 46 (2010) 703-719.
- [52] D. Wang, Z. Lin, Dispersion and transient analyses of Hermite reproducing kernel Galerkin meshfree method with sub-domain stabilized conforming integration for thin beam and plate structures, *Comput. Mech.* 48 (2011) 47-63.
- [53] S. Tanaka, S. Sadamoto, S. Okazawa, Nonlinear thin-plate bending analyses using Hermite reproducing kernel approximation, *Int. J. Comput. Meth.* 9 (2012) 1240012.
- [54] S. Tanaka, S. Sadamoto, S. Okazawa, Large deflection analysis for thin plates using the Hermite reproducing kernel (HRK) approximation, *Theor. Appl. Mech. Jpn.* 60 (2012) 205-214.
- [55] D. Wang, H. Peng, A Hermite reproducing kernel Galerkin meshfree approach for buckling analysis of thin plates, *Comput. Mech.* 51 (2013) 1013-1029.

- [56] K.M. Liew, J. Wang, T.Y. Ng, M.J. Tan, Free vibration and buckling analyses of shear-deformable plates based on FSDT meshfree method, *J. Sound. Vib.* 276 (2004) 997-1017.
- [57] K.M. Liew, X.L. Chen, J.N. Reddy, Mesh-free radial basis function method for buckling analysis of non-uniformly loaded arbitrarily shaped shear deformable plates, *Comput. Meth. Appl. Mech. Eng.* 193 (2004) 205-224.
- [58] K.M. Liew, X.L. Chen, Mesh-free radial point interpolation method for the buckling analysis of Mindlin plates subjected to in-plane point loads, *Int. J. Numer. Meth. Eng.* 60 (2004) 1861-1877.
- [59] K.M. Liew, X.L. Chen, Buckling of rectangular Mindlin plates subjected to partial in-plane edge loads using the radial point interpolation method, *Int. J. Solid. Struct.* 41 (2004) 1677-1695.
- [60] L.X. Peng, K.M. Liew, S. Kitipornchai, Buckling and free vibration analyses of stiffened plates using the FSDT mesh-free method, *J. Sound. Vib.* 289 (2006) 421-449.
- [61] K.M. Liew, L.X. Peng, S. Kitipornchai, Buckling analysis of corrugated plates using a mesh-free Galerkin method based on the first-order shear deformation theory, *Comput. Mech.* 38 (2006) 61-75.
- [62] K.M. Liew, L.X. Peng, S. Kitipornchai, Buckling of folded plate structures subjected to partial in-plane edge loads by the FSDT meshfree Galerkin method, *Int. J. Numer. Meth. Eng.* 65 (2006) 1495-1526.
- [63] L.W. Zhang, P. Zhu, K.M. Liew, Thermal buckling of functionally graded plates using a local Kriging meshless method, *Compos. Struct.* 108 (2014) 472-492.
- [64] T.Q. Bui, M.N. Nguyen, Ch. Zhang, Buckling analysis of Reissner-Mindlin plates subjected to in-plane edge loads using a shear-locking-free and meshfree method, *Eng. Anal. Bound. Elem.* 35 (2011) 1038-1053.
- [65] K.M. Liew, L.X. Peng, S. Kitipornchai, Geometric non-linear analysis of folded plate structures by the spline strip kernel particle method, *Int. J. Numer. Meth. Eng.* 71 (2007) 1102-1133.

- [66] K.M. Liew, L.X. Peng, S. Kitipornchai, Nonlinear analysis of corrugated plates using a FSDT and a meshfree method, *Comput. Meth. Appl. Mech. Eng.* 196 (2007) 2358-2376.
- [67] C. Murakami, M. Fujikubo, T. Yao, Influence of opening on elastic buckling strength of rectangular plates under single/combined loads, *Proc. 15th Asian TEAM on Marine Structures*, Jochiwon, Korea (2001) 114-123.

Appendix A. The formulas of perforated plate

- Longitudinal thrust

$a/b=2.0$
for $m=2$

$$R_{11} = \begin{cases} 1.108 - 0.108 \cos(\pi d/0.6b) & (d/b \leq 0.6) \\ 1.216 & (0.6 < d/b < 1.0) \end{cases} \quad (\text{A.1})$$

(A.2)

for $m=3-1$

$$R_{11} = \begin{cases} 1.014 + 0.161 \cos(\pi d/0.6b) & (d/b \leq 0.6) \\ 0.87 - 0.017 \cos\{\pi(d/b - 0.6)/0.6\} & (0.6 < d/b < 1.0) \end{cases} \quad (\text{A.3})$$

$a/b=3.0$

$$R_{11} = \begin{cases} 0.908 + 0.092 \cos(\pi d/0.5b) & (d/b \leq 0.5) \\ 0.9 - 0.084 \cos\{\pi(d/b - 0.5)/0.8\} & (0.5 < d/b < 1.0) \end{cases} \quad (\text{A.4})$$

- Transverse thrust

$a/b=2.0$

$$R_{22} = 0.934 - 0.132 \sin\{\pi(d/b - 0.2)/1.2\} \quad (\text{A.5})$$

$a/b=3.0$

$$R_{22} = 0.934 - 0.214 \sin\{\pi(d/b - 0.2)/2.0\} \quad (\text{A.6})$$

- Shear force $a/b=2.0$

$$R_{12} = \begin{cases} 0.81 + 0.2373 \cos\{\pi(d/b + 0.139)/0.678\} & (d/b \leq 0.2) \\ 0.81 - 0.56 \sin\{\pi(d/b - 0.2)/1.6\} & (0.2 < d/b < 1.0) \end{cases} \quad (\text{A.7})$$

$a/b=3.0$

$$R_{12} = \begin{cases} 0.78 + 0.22 \cos\{\pi d/0.6b\} & (d/b \leq 0.3) \\ 0.78 - 0.44 \sin\{\pi(d/b - 0.3)/1.2\} & (0.3 < d/b < 1.0) \end{cases} \quad (\text{A.8})$$